Quasimonoenergetic Proton Acceleration via Quantum Radiative Compression

Feng Wan[,1] Wei-Quan Wang,[2] Qian Zhao,[1] Hao Zhang,[2] Tong-Pu Yu[,2,*] Wei-Min Wang[,3] Wen-Chao Yan,[4,5] Yong-Tao Zhao[,1] Karen Z. Hatsagortsyan[,6] Christoph H. Keitel[,6] Sergei V. Bulanov[,7,8] and Jian-Xing Li[1,†]

[1] *MOE Key Laboratory for Nonequilibrium Synthesis and Modulation of Condensed Matter, School of Physics, Xi'an Jiaotong University, Xi'an 710049, China*

[2] *Department of Physics, National University of Defense Technology, Changsha 410073, China*

[3] *Department of Physics and Beijing Key Laboratory of Opto-electronic Functional Materials and Micro–nano Devices, Renmin University of China, Beijing 100872, China*

[4] *Key Laboratory for Laser Plasmas (MOE), School of Physics and Astronomy, Shanghai Jiao Tong University, Shanghai 200240, China*

[5] *Collaborative Innovation Center of IFSA (CICIFSA), Shanghai Jiao Tong University, Shanghai 200240, China*

[6] *Max-Planck-Institut für Kernphysik, Saupfercheckweg 1, Heidelberg 69117, Germany*

[7] *Institute of Physics ASCR, v.v.i. (FZU), ELI BEAMLINES, Za Radnicí 835, Dolní Břežany 252241, Czech Republic*

[8] *Kansai Photon Science Institute, National Institutes for Quantum and Radiological Science and Technology, 8-1-7 Umemidai, Kizugawa-shi, Kyoto 619-0215, Japan*

Dense high-energy monoenergetic proton beams are vital for wide applications, thus modern laser-plasma-based ion-acceleration methods are aiming to obtain high-energy proton beams with energy spread as low as possible. In this work, we put forward a quantum radiative compression method to postcompress a highly accelerated proton beam and convert it to a dense quasimonoenergetic one. We find that when the relativistic plasma produced by radiation-pressure acceleration collides head on with an ultraintense laser beam, large-amplitude plasma oscillations are excited due to quantum radiation reaction and the ponderomotive force, which induce compression of the phase space of protons located in its acceleration phase with negative gradient. Our three-dimensional spin-resolved quantum electrodynamics (QED) particle-in-cell simulations show that hollow-structure proton beams with a peak energy approximately GeV, relative energy spread of few percents, and number $N_p \sim 10^{10}$ (or $N_p \sim 10^9$ with a 1% energy spread) can be produced in near-future laser facilities, which may fulfill the requirements of alternative applications, such as, for radiography of ultrathick dense materials, or as injectors of hadron colliders.

I. INTRODUCTION

Laser-plasma-based ion acceleration can provide a much higher acceleration gradient (from GeV/m up to TeV/m), larger beam density (approximately 1% solid density), and shorter beam duration (fs–ps) than conventional electrostatic or radio-frequency accelerators [1,2], although the accelerated ion-beam qualities in terms of the energy spread and stability are worse. These ion sources are of paramount significance in broad applications, such as, material tomography [3,4], plasma radiography [5,6], cancer therapy [7–9], inertial confinement fusion (ICF) [10–12], and nuclear physics [13]. Generally, they require dense high-energy ion bunches with a rather low energy

spread, for instance, the energy spread of hundreds-of-MeV proton beam in the cancer therapy is limited to $\lesssim 1\%$ [2], that of hundreds-of-GeV (up to TeV) proton beam in the high-precision experiments of high-energy physics is approximately 10^{-4} [14,15], and the proton radiography resolution highly relies on the proton flux, energy, and spread [4]. Thus, dense high-energy monoenergetic proton beams are in great demand.

Recently, modern laser pulses have achieved a peak intensity of $I_0 \sim 10^{23}$ W/cm² with pulse duration of tens of femtoseconds [16–19]. Meanwhile, under construction or upgrading laser facilities, (e.g., ELI-beamlines [20], ELI-NP [21], SULF [22], Apollon [23], etc.) are aimed at $I_0 \gtrsim 10^{23}$ W/cm². With such intense lasers, the laser-plasma-based ion acceleration attracts broad attention. For instance, a hybrid scheme of radiation-pressure sheath acceleration is experimentally demonstrated, achieving

---

*tongpu@nudt.edu.cn
†jianxing@xjtu.edu.cn

024049-1

generation of proton beams with cutoff energy approximately 100 MeV, and with an exponentially rolling off plateau in the spectrum [24]. Collisionless shock acceleration can generate approximately 10^5 protons with a peak energy approximately 20 MeV and energy spread approximately 1% [25] (similarly, see Ref. [26]), while hole-boring radiation-pressure acceleration (RPA) at $I_0 \approx 10^{20}$ W/cm^2 can produce a maximal energy per nucleon $\lesssim 30$ MeV with energy spread approximately 30% [27–30]. By contrast, light-sail RPA [31], due to the advantages in the energy conversion and scaling, could generate much higher-energy protons (typically approximately GeV; further acceleration to tens of GeV might be influenced and even interrupted because of the Rayleigh-Taylor-like instability) with energy spread of tens of percents in three-dimensional (3D) simulations [those in less realistic two-dimensional (2D) simulations could be narrower] [32–39]. Notable, very recent experiment verifies that the light-sail RPA scheme can produce 10–30 MeV protons with CH targets of several nanometers [40]. Moreover, radiation reaction in the classical regime [41] may improve the quality of RPA beams [42,43]. As is known, in light-sail RPA to obtain GeV and even higher-energy protons, the energy scaling law requires $I_0 \gtrsim 10^{23}$ W/cm^2. In such an intense laser field though quantum radiation-reaction (QRR) effects [44], which have been observed recently in experiments [45,46], will play a significant role in the plasma dynamics [47–49]. For instance, the proton energy spectra can be essentially disturbed by the stochastic nature of photon emission [49]. Moreover, recent studies suggest that the electron and photon polarization can reshape QRR and related plasma dynamics [50–52]. Thus, the generation of dense GeV monoenergetic proton beams is still a great challenge.

In this paper, we put forward a quantum radiative compression (QRC) method to generate dense GeV quasi-monoenergetic proton beams. In addition to the common light-sail RPA, when a circularly polarized (CP) laser pulse irradiates an ultrathin target to generate and accelerate plasma, we apply another intense linearly polarized (LP) laser pulse head on colliding with the accelerated plasma after the first RPA stage [see Fig. 1(a)]. In the second stage, QRR dominates the plasma dynamics, inducing plasma oscillations with the assistance of the laser ponderomotive force. Consequently, an oscillating longitudinal electric field $E_{z,\text{osci.}}$ inside the plasma is excited and further accelerates and compresses protons to form a dense quasimonoenergetic proton beam: initially lower-energy protons experience a larger acceleration force F to gain more energy and thus catch up initially higher-energy ones (resulting in rotation of the phase space) [see Figs. 1(b) and 1(c) and detailed explanations in Figs. 2 and 3]. We underline that in the QRC process the scattering laser and QRR are indispensable (see Fig. 4). To describe the plasma dynamics accurately in the applied QRR regime,
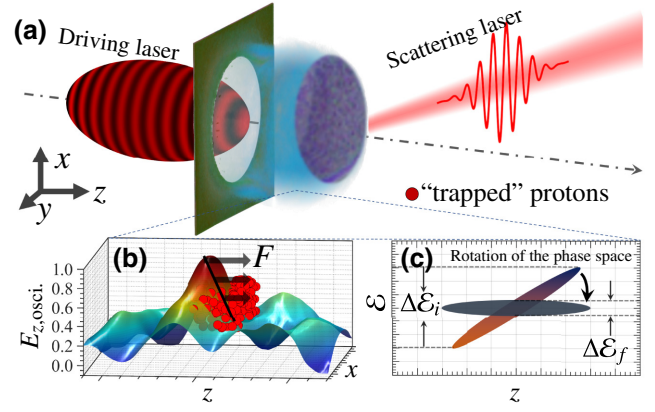

FIG. 1. Interaction scenario. (a) The accelerated plasma via light-sail RPA by a CP driving laser collides with another LP scattering laser after RPA. (b) Protons are "trapped" and further accelerated by the oscillating longitudinal field $E_{z,\text{osci.}}$, induced by QRR effects and the ponderomotive force. The black line and arrows represent the negative gradient of $E_{z,\text{osci.}}$ and the acceleration force F, respectively. Longer arrows denote larger F. (c) The energy spread of protons is compressed.

we have implemented the spin-resolved Monte Carlo processes of electron dynamics and radiation [52–56] into the 3D particle-in-cell (PIC) code EPOCH [57]. With upcoming laser facilities [16–20,23,58], proton bunches with a peak energy of GeV order, relative energy spread of few percents and total number $N_p \sim 10^{10}$ can be obtained (see Fig. 4), to the benefit of many applications.

II. SIMULATION PARAMETERS AND MAIN RESULTS

Sample results of generated dense GeV quasimonoenergetic proton beams are illustrated in Fig. 4. When choosing the laser and plasma parameters we ensure fulfilling the conditions for the relativistic transparency and light-sail RPA, as follows. The peak intensity of the CP driving laser is $I_{d0} \approx 8.56 \times 10^{22}$ W/cm^2 (invariant parameter $a_{d0} = eE_0/m_e c\omega_d \approx 250$ with wavelength $\lambda_d = 1$ μm). $-e$ and m_e are the charge and mass of electron, respectively, E_0 and ω_d the amplitude and frequency of the driving laser, respectively, and c the light speed in vacuum. The laser profile is $\frac{1}{2}\exp\left(-r^4/w_{d0}^4\right)\{\tanh[2(t-t_1/T_0)] - \tanh[2(t-t_2/T_0)]\}$ with focal radius $w_{d0} = 6$ μm. $t_1 = 88T_0$ and $t_2 = 98T_0$ are the times of the front and tail of the driving laser entering the simulation box, respectively, with laser period T_0, and the pulse duration $\tau_d = t_2 - t_1$. We consider a fully ionized polystyrene target composed of e^-, C^{6+}, and H^+, with number densities $n_e(e^-) = 300n_c$ and $n_p(H^+) = n_C(C^{6+}) = n_e(e^-)/7$, and target thickness $l = 0.3$ μm. $n_c = m_e\omega_d^2/4\pi e^2$ is the critical plasma density. The laser and target parameters are optimized to meet the partially relativistic transparency condition $l/\lambda_d \approx a_{d0}n_c/\pi n_e \approx 0.3$ [59,

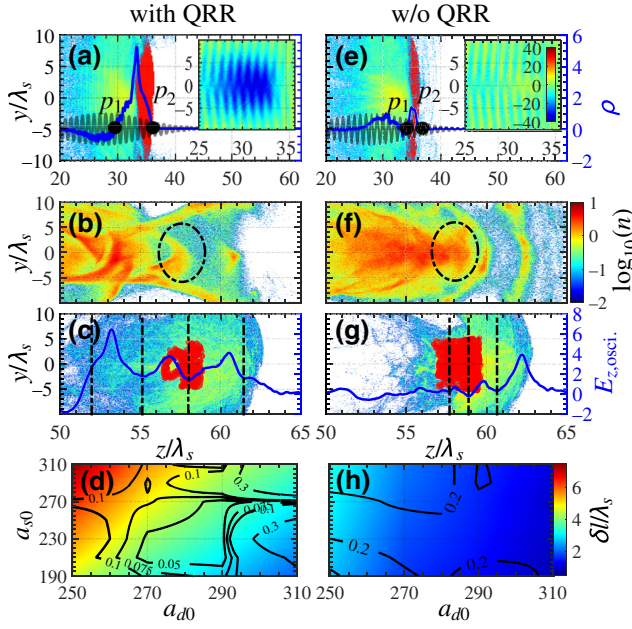FIG. 2. (a),(e) Number density distributions of ions ($6n_C + n_p$, red) and electrons (n_e, colored background) at $t = 66T_0$. To show the relative slippage between electrons and ions, here ions are partially shaded by electrons. Solid-gray and solid-blue curves indicate normalized scattering laser profile and charge density ρ on the propagation axis ($y = 0$), respectively. Black dots denote $\rho(p_1) = \rho(p_2) = 0$, and the relative slippage distance between the electron and ion layer is defined as $\delta l \equiv z(p_2) - z(p_1)$. Subfigures show E_z. (b),(f) n_e at $t = 94T_0$. Black-dashed circles denote the positions of traced protons. (c),(g) n_p at $t = 94T_0$. Traced protons within $\Delta\mathcal{E}$ are labeled in red. Solid-blue curves denote $E_{z,\text{osci.}}$ on the propagation axis ($y = 0$). (b),(c) and (f),(g) share the same color bar. (d),(h) Correlation between δl (hot map) and $\Delta\mathcal{E}/\mathcal{E}_{\text{peak}}$ (contour) with respect to a_{d0} and a_{s0}. Left and right columns show the cases including and excluding QRR, respectively, with the scattering laser. Here 2D simulations are employed for simplicity. Other parameters are the same as those in Fig. 4. Note that E and B are normalized by $e/m_e c\omega_s$, n by n_c, and ρ by $n_c e$.

60], which can suppress the target-deformation-induced instability [61]. For the LP scattering laser, $I_{s0} \approx 8.56 \times 10^{22}$ W/cm^2 ($a_{s0} = 250$) with wavelength $\lambda_s =$
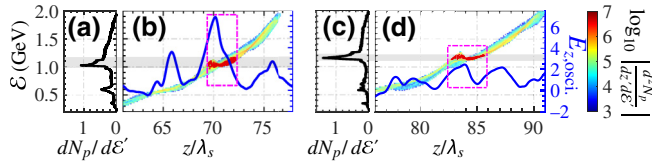

FIG. 3. (a),(c) $dN_p/d\mathcal{E}'$ normalized by a factor of 9.39×10^{16} vs $\mathcal{E}$ at $t = 114T_0$ and $t = 130T_0$, respectively. $\mathcal{E}' \equiv \mathcal{E}/\text{GeV}$. (b),(d) $\log_{10}(d^2N_p/dz'd\mathcal{E}')$ with respect to $z' = z/\lambda_s$ and $\mathcal{E}$ at $t = 114T_0$ and $t = 130T_0$, respectively. The blue lines and red particles indicate $E_{z,\text{osci.}}$ ($y = 0$) and traced protons, respectively. Other parameters are the same as those in Fig. 2.
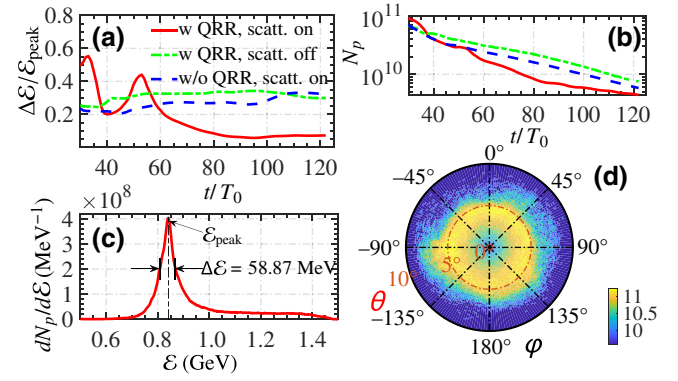

FIG. 4. (a),(b) Time evolutions of the relative energy spread $\Delta\mathcal{E}/\mathcal{E}_{\text{peak}}$ and number N_p of the protons collected from the cylinder with a 7-μm radius along the propagating axis, respectively. $\Delta\mathcal{E}$ is the FWHM of the density spectrum [see (c)]. The red-solid, green-dash-dotted, and blue-dashed curves indicate the cases including QRR and scattering laser, including QRR but no scattering laser, and including scattering laser but no QRR, respectively. Here $t = 0$ is redefined as the time of the driving laser reaching the left boundary of the simulation box. (c),(d) For the case including QRR and scattering laser, $dN_p/d\mathcal{E}$ (MeV^{-1}) and $\log_{10}(d^2N_p/d\theta d\phi)$ at $t = 98T_0$. θ and ϕ are the polar and azimuthal angles, respectively. The 3D simulation box is placed at $-20\ \mu$m $\leq z \leq 100\ \mu$m, $-15\ \mu$m $\leq x \leq 15\ \mu$m and $-15\ \mu$m $\leq y \leq 15\ \mu$m, with mesh size $n_z \times n_x \times n_y = 6000 \times 300 \times 300$. The target is placed at $-18.65\ \mu$m $\leq z \leq -18.35\ \mu$m and represented by 150 macroelectrons, 50 macroprotons, and 10 macrocarbon ions per cell. Other parameters are given in the text.

λ_d, and the profile $\frac{1}{2} \exp\left(-r^2/w_{s0}^2\right)\{\tanh[2(t - t_3/T_0)] - \tanh[2(t - t_4/T_0)]\}$ with focal radius $w_{s0} = 7\ \mu$m, $t_3 = 3T_0$, $t_4 = 19T_0$, and duration $\tau_s = t_4 - t_3$. These synchronized laser beams will be feasible soon by splitting one laser beam in multipetawatt facilities [17–20,23,58].

During light-sail RPA the electrons are accelerated to the average energy of about 50 MeV (Lorentz factor $\gamma_e \approx 100$); see the energy spectrum of electrons before colliding with the scattering laser in Fig. 5. Afterwards, they collide with the scattering laser to emit photons via nonlinear Compton scattering. The strong field quantum parameter is $\chi_e = (\hbar\omega_s/m_e c^2)\gamma_e a_{s0}[1 - v_e \cos(\theta_{\text{coll.}})/c] \sim 0.01 - 0.1$, which indicates that QRR is not negligible, however, further electron-positron pair production via nonlinear Breit-Wheeler process is suppressed [44,62]. Here v_e is the electron velocity, $\theta_{\text{coll.}}$ the collision angle, and $\hbar$ the reduced Planck constant. Our analysis in Figs. 2 and 3 shows that indeed the electron motion is affected by QRR, and what is more remarkable, it has significant consequences for the ion dynamics due to the modification of charge-separation forces.

As shown in Figs. 4(a) and 4(b), as including the scattering laser and QRR, before $t \approx 33T_0$, the relative energy spread of the protons $\Delta\mathcal{E}/\mathcal{E}_{\text{peak}}$ first increases since the
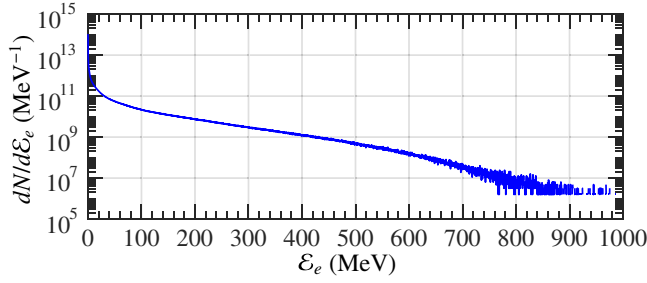
FIG. 5.   Energy spectrum of electrons at $t = 22T_0$ (before colliding head on with the scattering laser). Other parameters are the same as those in Fig. 4.

FIG. 6.   Phase-space evolution of protons before the QRC process: (a1), (b1), and (c1) show the normalized energy spectra $dN'_p/d\mathcal{E}$ vs $\mathcal{E}$ at $t = 40T_0, t = 45T_0$ and $t = 50T_0$, respectively. (a2), (b2), and (c2) show $\log_{10}(d^2N_p/dz'd\mathcal{E}')$ with respect to z and $\mathcal{E}$ at $t = 40T_0, t = 45T_0$ and $t = 50T_0$, respectively. Here, $z' = z/\lambda_s$ and $\mathcal{E}' = \mathcal{E}/\text{GeV}$. The gray bands denote the FWHM of the energy spectra. Other parameters are the same as those in Fig. 4 in the paper.

scattering laser pushes the electrons and consequently increases $\Delta\mathcal{E}$ by charge-separation forces; in $33T_0 \lesssim t \lesssim 53T_0$ instead $\Delta\mathcal{E}/\mathcal{E}_{\text{peak}}$ is unstable because even though the scattering laser has left the protons are not stably phase matched with the excited oscillating longitudinal field $E_{z,\text{osci.}}$ (see the phase-space evolution of protons before the QRC process in Fig. 6); after $t \approx 53T_0$, $E_{z,\text{osci.}}$ is becoming stable, and the protons are gradually phase matched with $E_{z,\text{osci.}}$ and substantially compressed by $E_{z,\text{osci.}}$ (negative gradient) from initial $\Delta\mathcal{E}/\mathcal{E}_{\text{peak}} \gtrsim 40\%$ down to $\lesssim 6\%$ (see physical reasons in Figs. 2 and 3). The proton number N_p is continuously reduced due to the transverse momenta. In contrast, as excluding the scattering laser (common setup) or artificially removing QRR (in which electron dynamics is governed by the Lorentz force, and the electron spin by the Thomas-Bargmann-Michel-Telegdi equation [63–65]), $\Delta\mathcal{E}/\mathcal{E}_{\text{peak}}$ is always large (approximately 25%–35%). Thus, QRR and the ponderomotive force result in the generation of a quasimonoenergetic proton beam; see specific results in Figs. 4(c) and 4(d). The peak energy is $\mathcal{E}_{\text{peak}} \approx 839$ MeV with $\Delta\mathcal{E}/\mathcal{E}_{\text{peak}} \approx 6\%$, $N_p \approx 4.6 \times 10^9$, and radial angular divergence $\theta \approx 68$ mrad (about 3.9°). And, one obtains $N_p \approx 10^9$ within 1% energy spread at $\mathcal{E}_{\text{peak}}$. Such a proton beam may serve as an injector for a hadron collider or ion radiography source for ultrathick targets [2,66].

Moreover, the proton beam has a hollow structure [see Fig. 4(d)], which may find an application as a high-energy positron collimator [67]. Note that here the spin effects on the proton dynamics are insignificant, in contrast to Refs. [52,55,62], since the employed target is not spin polarized and consequently the particle spin effects on their dynamics cancel each other out, and the pair production is negligible.

III. DISCUSSION AND ANALYSIS

The physics behind the proton QRC process is analyzed in Figs. 2 and 3. Due to the relativistic transparency effects and Rayleigh-Taylor-like instability, the driving laser penetrates through the electron layer and induce an
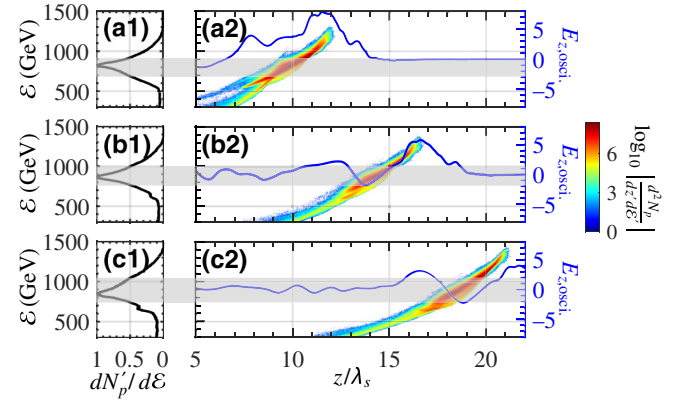
energy spread of accelerated protons [31,32]. When the scattering laser collides head on with the plasma, the electrons are decelerated and left behind the protons with a slippage distance δl, and the charge separation between electrons and protons along with the current flow can excite a strong longitudinal electric field $E_z = E_{z,\text{stat.}} + E_{z,\text{curr.}} < 0$ [see Fig. 2(a)]. Here the current-flow-induced $E_{z,\text{curr.}} > 0$ is mainly derived from those protons moving faster than electrons, and $E_{z,\text{curr.}}$ reduces $|E_z|$ (the charge-separation field $E_{z,\text{stat.}} < 0$). When the scattering laser left, the electrons will be reaccelerated by $E_z < 0$ and excite a plasma oscillation $E_{z,\text{osci.}}$ [see Figs. 2(b) and 2(c)]. The protons synchronized with its negative-gradient phase ($E_{z,\text{osci.}} > 0$, $\partial_z E_{z,\text{osci.}} < 0$) can be "trapped" and experience an energy-dependent acceleration field [see Fig. 2(c) and the scenario in Figs. 1(b) and 1(c)]. For instance, the protons locating near $z \approx 56.6\lambda_s$ are subjected to $E_{z,\text{osci.}} \approx 4.0$, which is stronger than $E_{z,\text{osci.}} \approx 1.7$ near $z \approx 58\lambda_s$. Since lower-energy protons move relatively slower than higher-energy ones and thus are at the rear, $E_{z,\text{osci.}}$ with negative-gradient can provide stronger acceleration for lower-energy protons near $z \approx 56.6\lambda_s$. Thus, the protons can be compressed in energy space [see Fig. 3]. The detailed evolutions of proton phase space in the QRC process with the scattering laser, for the cases of including and excluding the QRR effects, are illustrated in Fig. 7, and the comparison between these two cases can clearly show the impact of the QRR effects on the QRC process.

Note that the compression efficiency is determined by $E_{z,\text{osci.}}$ and its spatial gradient $\partial_z E_{z,\text{osci.}}$, relying on E_z, and the oscillation wavelength is $\lambda_{\text{osci.}} \sim \delta l$. Since $E_z = E_{z,\text{stat.}} + E_{z,\text{curr.}}$ and $E_{z,\text{stat.}} \propto \delta l$, thus δl plays a key role
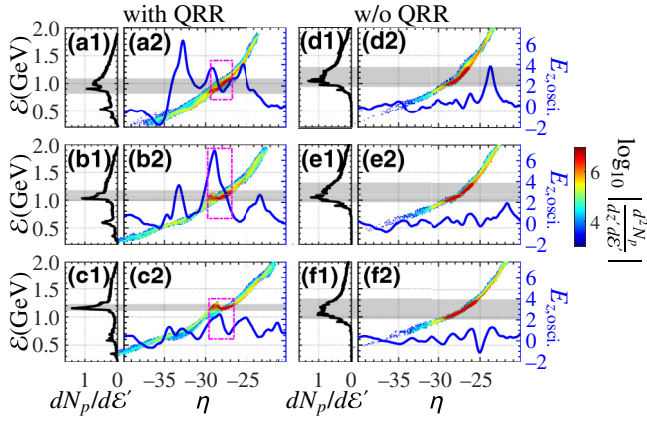
FIG. 7. Simulations including the scattering laser and QRR effects: (a1), (b1), and (c1) show the energy spectra $dN_p/d\mathcal{E}'$ normalized by a factor of 9.39×10^{16} vs $\mathcal{E}$ at $t = 94T_0$, $t = 114T_0$ and $t = 130T_0$, respectively; (a2), (b2), and (c2) show $\log_{10}\left[d^2N_p/dz'd\mathcal{E}'\right]$ with respective to $\eta = k_sz - \omega_st$ and $\mathcal{E}$ at $t = 94T_0$, $t = 114T_0$ and $t = 130T_0$, respectively. Simulations including the scattering laser but not QRR effects: (d1), (e1), and (f1) show the energy spectra $dN_p/d\mathcal{E}'$ normalized by a factor of 9.39×10^{16} vs $\mathcal{E}$ at $t = 94T_0$, $t = 114T_0$, and $t = 130T_0$, respectively; (d2), (e2), and (f2) show $\log_{10}\left[d^2N_p/dz'd\mathcal{E}'\right]$ with respective to η and $\mathcal{E}$ at $t = 94T_0$, $t = 114T_0$, and $t = 130T_0$, respectively. Here, $z' = z/\lambda_s$ and $\mathcal{E}' = \mathcal{E}/\text{GeV}$. The gray bands denote the FWHM of the energy spectra. Other parameters are the same as those in Fig. 4.

in the excitation of $E_{z,\text{osci.}}$, induced by the ponderomotive force F_p and QRR force F_{QRR} [68] (see details in the Appendix). Here, F_p in z direction is given by $F_{p,z} \simeq -2/\pi(1 + c/v_z)\partial_\eta a_s$ [69,70] (see details in the Appendix), where $a_s(\eta)$ is instantaneous field parameter with $\eta = k_sz - \omega_st$ and $k_s = 2\pi/\lambda_s$. For given parameters, $\max(F_{p,z}) \approx 4a_{s0}/\pi\tau_s\sqrt{2/e'} = 4.4$, where e' is the natural logarithm base. While, the QRR force can be estimated via $F_{\text{QRR}} \simeq -2/3\chi_e^2\alpha_f^2(\lambda_s/r_e)g(\chi_e)$ [71–73], where $g(\chi_e) \simeq (1 + 8.93\chi_e + 2.41\chi_e^2)^{-2/3}$ is the quantum suppression function, α_f the fine structure constant and r_e the classical electron radius. By averaging over a scattering laser period, $\langle F_{\text{QRR}} \rangle \approx -4/3\pi\chi_e'^2\alpha_f^2(\lambda_s/r_e)g(\chi_e')$, where $\chi_e' \approx (2\hbar\omega_s\gamma_ea_{s0}/m_ec^2)\exp\left(-\eta^2/\tau_s^2\right)$. For $\langle\gamma_e\rangle \approx 70$, $\max\{\langle F_{\text{QRR}}\rangle\} \approx 27$, which is much larger than $\max(F_{p,z})$. Those two forces are balanced by the excited longitudinal field: $|E_z| \approx |F_{p,z} + F_{\text{QRR}}|$. From the simulation results [see E_z in Fig. 2(a)] $\max(|E_z|) \approx 40$ is very close to the estimated $\max(|F_{p,z} + F_{\text{QRR}}|) \approx 32$. We have also estimated $\max\left(E_{z,\text{stat.}}\right) = E_{z,\text{stat.}}(p_1) = -\int_{z(p_2)}^{z(p_1)}\rho(z)dz \simeq \rho_{\max}\delta l/2 \approx -20\pi$ with $\rho_{\max} \approx 4$ and $\delta l \approx 5\lambda_s$, which is in fact larger than $|E_z|$ due to counteracting $E_{z,\text{curr.}} > 0$. The QRC is caused by the excited oscillation field $E_{z,\text{osci.}} \approx 4-5$ with $\lambda_{\text{osci.}} \approx 3\lambda_s$ [see Fig. 2(c)]. The phase space of those "trapped" protons continuously rotates [see Figs. 3(b) and 3(d)], and the energy spread

is reduced approximately from 200 MeV at $t = 114T_0$ to 100 MeV at $t = 130T_0$ [see Figs. 3(a) and 3(c)]. These compression effects can sustain about 10–30 periods and the final energy spread can be compressed down to few percents [see Fig. 2(d)].

As given in the applied condition $F_{\text{QRR}} \gg F_{p,z}$, the key role of QRR for the QRC process is clear, which is described by the QRC parameter $|F_{\text{QRR}}/F_{p,z}| \sim \mathcal{R} \equiv (\chi^2\lambda_s\tau_s/a_{0s})(\alpha^2/r_e)$. In fact, as we artificially remove QRR, the compression effects will be greatly suppressed [see Figs. 2(e)–2(h)]. In this case $E_{z,\text{peak}} \approx \max\left(F_{p,z}\right) \approx 5$ and $\delta l \approx 3\lambda_s$ [see Fig. 2(e)]. $E_{z,\text{osci.}} \approx 1.0$ with $\lambda_{\text{osci.}} \approx \lambda_s$ [see Fig. 2(g)]. And the final compression effects are rather weak [see Fig. 2(h)].

IV. EXPERIMENTAL FEASIBILITY

For the experimental feasibility, we investigate the impact of the driving and scattering laser parameters on the QRC efficiency [see Fig. 8]. As $190 \le a_{s0} \le 280$, $\max(\chi_e) \approx 0.05 \sim 0.07$ and $F_{\text{QRR}} \approx 26.8 - 33.1$, which is still much larger than $F_{p,z}$, and QRC takes place. While at smaller a_{s0} the QRC is suppressed, at larger a_{s0} the QRC will be enhanced up to the point when δl is comparable to the longitudinal thickness of the plasma. In deep quantum regime with $\chi_e(\propto a_{s0}) \gg 1$, the quantum stochasticity would induce beam spreading [74]. From $\mathcal{R}$ we can deduce that τ_s plays a similar role as a_{s0} [see Figs. 8(a) and 8(b)]. Moreover, the driving laser determines the energies of electrons and protons in light-sail RPA and therefore affects many parameters, e.g., χ_e, n_e, and n_i. As expected, $\mathcal{E}_{\text{peak}}$ is proportional to a_{d0} and τ_d. However, when a_{d0} is much lower than the transparency condition ($a_{d0} \ll \pi n_el/n_c\lambda_d$) [75,76], γ_e and χ_e will be much smaller, and consequently F_{QRR} is rather weak and the QRC will be ineffective. In contrast, if a_{d0} is too high, the target deformation will be much earlier, which will also limit the effective acceleration [see Fig. 8(c)]. τ_d has similar effects: a too short driving laser can not effectively accelerate plasma, while a too long driving laser will generate very high-energy protons, which are hard to compress due to limited $E_{z,\text{osci.}}$ and $\lambda_{\text{osci.}}$ [see Fig. 8(d)]. Note that these results are collected at $t = 130T_0$, and for longer pulses the energy spectra may be further compressed when extending the simulation sizes. The results of QRC with the laser parameters in ELI-NP [21] are given in Figs. 8(e) and 8(f), where intensity $I_{d0} \approx 1.0 \times 10^{23}$ W/cm^2 ($a_{d0} \approx 215$), wavelengths $\lambda_d = \lambda_s = 0.8$ μm, pulse durations $\tau_d = \tau_s = 16$ fs $\approx 6T_0$, spot sizes $w_{d0} = w_{s0} = 3.5$ μm, and energy $\mathcal{E} \simeq 225$ J. Even though the laser pulse durations τ_d and τ_s are much smaller than the optimal regimes in Figs. 8(b) and 8(d), the QRC can still compress the energy spread significantly, for instances, from over 100% to about 5.2%, 6.6%, 5.7%, 4.6%, and 6.2% with $a_{s0} = 205$, 215, 225,
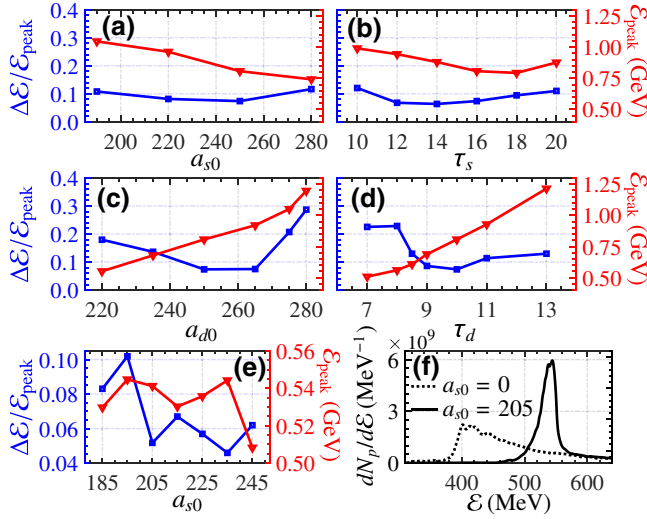
FIG. 8. (a)–(d) Impacts of a_{s0}, τ_s, a_{d0}, and τ_d on $\mathcal{E}_{\text{peak}}$ and $\Delta\mathcal{E}/\mathcal{E}_{\text{peak}}$, respectively. Other parameters are the same as those in Fig. 4. (e),(f) $\Delta\mathcal{E}/\mathcal{E}_{\text{peak}}$ and $\mathcal{E}_{\text{peak}}$ vs a_{s0}, and $dN_p/d\mathcal{E}$ (MeV^{-1}) vs $\mathcal{E}_p$ (MeV), respectively, employing the laser parameters in ELI-NP [21]. In (f), the solid and dotted lines indicate the cases of including and excluding the scattering laser, with $\Delta\mathcal{E}/\mathcal{E}_{\text{peak}} \lesssim$ 6% and $\gtrsim$ 25%, respectively. Other parameters are given in the text.

235, and 245, respectively; see Fig. 8(e). Thus, our proposed QRC scheme may be observed in ELI-NP and other similar facilities.

V. CONCLUSION

In summary, we propose the QRC method to generate dense GeV quasimonoenergetic proton beams, which is based on QRR effects for proton dynamics in plasma. With up-coming laser facilities, such as ELI-beamlines, SULF, Appolon, hollow-structure proton beams with peak energy $\mathcal{E}_{\text{peak}} \sim$ GeV, energy spread $\lesssim$ 6%, and number $N_p \sim 10^{10}$ ($N_p \sim 10^9$ within $\Delta\mathcal{E}/\mathcal{E}_{\text{peak}} \leq 1\%$) can be obtained, which may fulfill the requirements of high-resolution proton imaging, high-energy particle physics, and relativistic positron collimation.

APPENDIX

The relativistic corrected ponderomotive force for linearly polarized laser with invariant intensity parameter a can be estimated as follows:

$$\mathbf{F}_p = -\frac{m_e c^2}{4\pi}\frac{\nabla a^2}{\sqrt{1+a^2}}$$
$$\left[\left(\frac{1}{a^2}+1\right)E(2\pi,\kappa)-\frac{1}{a^2}F(2\pi,\kappa)\right],$$

where $\kappa = a/\sqrt{1+a^2}$, $F(\phi,\kappa)$, and $E(\phi,\kappa)$ are the incomplete integrals of the second and first kind of elliptic functions. When $a \gg 1$,

$$\left[\left(\frac{1}{a^2}+1\right)E(2\pi,\kappa)-\frac{1}{a^2}F(2\pi,\kappa)\right]\simeq 4,$$

$\mathbf{F}_p$ can be simplified as

$$\mathbf{F}_p \simeq -\frac{mc^2}{\pi}\frac{\nabla a^2}{\sqrt{1+a^2}}$$

and the normalized version is

$$\mathbf{F}_p \simeq -\frac{1}{\pi}\frac{\nabla a^2}{\sqrt{1+a^2}}.$$

Thus, the longitudinal components can be expressed as

$$F_{p,z} \simeq -\frac{1}{\pi}\frac{\partial_z a^2}{\sqrt{1+a^2}}$$
$$= -\frac{1}{\pi}\frac{\partial_\eta a^2}{\sqrt{1+a^2}}\partial_z\eta$$
$$\simeq -\frac{2}{\pi}\frac{\partial\eta}{\partial z}\partial_\eta a = -\frac{2}{\pi}(1+\beta_z^{-1})\partial_\eta a,$$

where β_z is the electron velocity scaled by the light speed in vacuum c, $\eta = z + t$ and $\partial_z\eta = 1 + (\partial z/\partial t)^{-1}$. Here, z and t are normalized by k and ω, respectively.

The dynamics of a single electron in plane-wave field can be expressed as follows:

$$\mathbf{p} = \mathbf{p}_0 - \frac{e}{c}\mathbf{A}(\tau) + \boldsymbol{v}_0\frac{e^2 A^2(\tau)-2ec[\mathbf{p}_0\mathbf{A}(\tau)]}{2c\Lambda}, \quad (A1)$$

$$\mathbf{x} = \mathbf{x}_0 + \frac{c^2\mathbf{p}_0}{\Lambda}(\tau-\tau_0) + \frac{c}{\Lambda}\int_{\tau_0}^{\tau}$$
$$\times\left\{\frac{\boldsymbol{v}_0}{2\Lambda}\left[e^2 A^2(\tau')-2ec\mathbf{p}_0\mathbf{A}(\tau')\right]-e\mathbf{A}(\tau')\right\}d\tau',$$
$$(A2)$$

where $\mathbf{p}_0$ is the initial momentum of electron, $\boldsymbol{v}_0$ the propagation direction vector of the laser, $\mathbf{A}(\tau)$ the vector

potential of the laser field, $\tau \equiv t - \nu_0 \mathbf{x}/c$ the phase of electron in the laser field, $\Lambda \equiv \mathcal{E}_0 - c\mathbf{p}_0\nu_0$ a constant integral of the electron motion, $-e$ and c the electron charge and light speed in vacuum, respectively, $\mathcal{E}_0$ the initial electron energy. Thus, the longitudinal slippage distance caused by the linearly polarized scattering laser can be easily obtained from Eq. (A2) as

$$\delta l = \mathbf{x}_{\parallel} - \mathbf{x}_{\parallel}(\mathbf{A} = 0) = \frac{c}{2\Lambda^2}\int_{\tau_0}^{\tau} e^2 A^2(\tau')d\tau', \quad \text{(A3)}$$

where $\mathbf{p}_0 \parallel \nu_0 \perp \mathbf{A}(\tau)$ is used. For a Gaussian laser pulse with a long pulse duration $\Delta\tau \gg T_0$, $\mathbf{A}(\tau) = -c\int_{-\infty}^{\tau}\mathbf{E}(\omega\tau')\cos\omega\tau'd\tau' \simeq -c[\mathbf{E}(\omega\tau)/\omega]\sin\omega\tau$, and

$$\begin{aligned}\delta l &\simeq \frac{c^3 e^2}{2\Lambda^2\omega^2}\int_{-\infty}^{\infty}\mathbf{E}^2(\omega\tau')\tan^2\omega\tau'd\tau'\\ &= \frac{c^3 e^2}{2\Lambda^2\omega^3}\int_{-\infty}^{\infty}\mathbf{E}^2(\phi)\tan^2\phi d\phi\\ &= \frac{c^3 e^2}{8\gamma_0^2\omega^2 m^2 c^4}\int_{-\infty}^{\infty}\mathbf{E}^2(\phi)\tan^2\phi d\tau'\\ &= \frac{\pi e^2}{2\gamma_0^2 m^2 c^2\omega^2}\int_{-\infty}^{\infty}I(\phi)d\tau'\\ &\simeq \frac{\alpha_f c\hbar\pi}{2\gamma_0^2 m^2 c^2\omega^2}\frac{\mathcal{E}_{\text{laser}}}{\sigma}\\ &= \frac{\alpha_f \lambdabar_c}{8\pi\gamma_0^2}\frac{\mathcal{E}'}{\sigma'},\end{aligned}\quad\text{(A4)}$$

where $\mathcal{E}' \equiv \mathcal{E}_{\text{laser}}/mc^2$ with laser energy $\mathcal{E}_{\text{laser}}$, $\sigma' \equiv \sigma/\lambda_0^2$ with the laser spot area σ, the laser wave vector $k = \omega/c = 2\pi/\lambda_0$, reduced Compton wavelength $\lambdabar_c = \hbar/m_e c$, fine structure constant $\alpha_f = e^2/c\hbar$, and the Lorentz factor of electron $\gamma_0 \gg 1$ is assumed. With those parameters given in the paper, we can obtain via Eq. (A4) $\delta l \simeq \lambda_0$.

———————

[1] G. A. Mourou, T. Tajima, and S. V. Bulanov, Optics in the relativistic regime, Rev. Mod. Phys. **78,** 309 (2006).

[2] A. Macchi, M. Borghesi, and M. Passoni, Ion acceleration by superintense laser-plasma interaction, Rev. Mod. Phys. **85,** 751 (2013).

[3] M. Roth, A. Blazevic, M. Geissel, T. Schlegel, T. E. Cowan, M. Allen, J.-C. Gauthier, P. Audebert, J. Fuchs, J. M. ter Vehn, M. Hegelich, S. Karsch, and A. Pukhov, Energetic ions generated by laser pulses: A detailed study on target properties, Phys. Rev. ST Accel. Beams **5,** 061301 (2002).

[4] M. Borghesi, A. J. Mackinnon, D. H. Campbell, D. G. Hicks, S. Kar, P. K. Patel, D. Price, L. Romagnani, A. Schiavi, and O. Willi, Multi-MeV Proton Source Investigations in Ultraintense Laser-Foil Interactions, Phys. Rev. Lett. **92,** 055003 (2004).

[5] M. Borghesi, D. H. Campbell, A. Schiavi, M. G. Haines, O. Willi, A. J. MacKinnon, P. Patel, L. A. Gizzi, M. Galimberti, R. J. Clarke, F. Pegoraro, H. Ruhl, and S. Bulanov, Electric field detection in laser-plasma interaction experiments via the proton imaging technique, Phys. Plasmas **9,** 2214 (2002).

[6] A. J. Mackinnon, *et al.*, Proton Radiography of a Laser-Driven Implosion, Phys. Rev. Lett. **97,** 045001 (2006).

[7] S. V. Bulanov and V. S. Khoroshkov, Feasibility of using laser ion accelerators in proton therapy, Plasma Phys. Rep. **28,** 453 (2002).

[8] D. Schardt, T. Elsässer, and D. Schulz-Ertner, Heavy-ion tumor therapy: Physical and radiobiological benefits, Rev. Mod. Phys. **82,** 383 (2010).

[9] S. V. Bulanov, J. J. Wilkens, M. Molls, T. Z. Esirkepov, G. Korn, G. Kraft, S. D. Kraft, and V. S. Khoroshkov, Laser ion acceleration for hadron therapy, Phys. Uspekhi **57,** 1149 (2014).

[10] M. Roth, T. E. Cowan, M. H. Key, S. P. Hatchett, C. Brown, W. Fountain, J. Johnson, D. M. Pennington, R. A. Snavely, S. C. Wilks, K. Yasuike, H. Ruhl, F. Pegoraro, S. V. Bulanov, E. M. Campbell, M. D. Perry, and H. Powell, Fast Ignition by Intense Laser-Accelerated Proton Beams, Phys. Rev. Lett. **86,** 436 (2001).

[11] N. Naumova, T. Schlegel, V. T. Tikhonchuk, C. Labaune, I. V. Sokolov, and G. Mourou, Hole Boring in a DT Pellet and Fast-Ion Ignition with Ultraintense Laser Pulses, Phys. Rev. Lett. **102,** 025002 (2009).

[12] V. Tikhonchuk, T. Schlegel, C. Regan, M. Temporal, J.-L. Feugeas, P. Nicolaï, and X. Ribeyre, Fast ion ignition with ultra-intense laser pulses, Nucl. Fusion **50,** 045003 (2010).

[13] A. Macchi, A. Sgattoni, S. Sinigardi, M. Borghesi, and M. Passoni, Advanced strategies for ion acceleration using high-power lasers, Plasma Phys. Control Fusion **55,** 124020 (2013).

[14] CERN, Large Hadron Colliders (LHC), https://home.cern/science/accelerators/large-hadron-collider.

[15] RHIC (Relativistic Heavy Ion Colliders), https://www.bnl.gov/rhic/.

[16] J. W. Yoon, Y. G. Kim, I. W. Choi, J. H. Sung, H. W. Lee, S. K. Lee, and C. H. Nam, Realization of laser intensity over 10^{23} W/cm², Optica **8,** 630 (2021).

[17] J. W. Yoon, C. Jeon, J. Shin, S. K. Lee, H. W. Lee, I. W. Choi, H. T. Kim, J. H. Sung, and C. H. Nam, Achieving the laser intensity of 5.5×10^{22} W/cm² with a wavefront-corrected multi-PW laser, Opt. Express **27,** 20412 (2019).

[18] C. N. Danson, *et al.*, Petawatt and exawatt class lasers worldwide, High Power Laser Sci. Eng. **7,** e54 (2019).

[19] S. Gales, *et al.*, The extreme light infrastructure—nuclear physics (ELI-NP) facility: New horizons in physics with 10 PW ultra-intense lasers and 20 meV brilliant gamma beams, Rep. Progr. Phys. **81,** 094301 (2018).

[20] The Extreme Light Infrastructure (ELI), http://www.eli-beams.eu/en/facility/lasers/.

[21] K. A. Tanaka, *et al.*, Current status and highlights of the ELI-NP research program, Matter Radiat. Extremes **5,** 024402 (2020).

[22] Z. Gan, *et al.*, in *Progress in Ultrafast Intense Laser Science XVI*, edited by K. Yamanouchi, K. Midorikawa, and L. Roso (Springer International Publishing, Cham, 2021), p. 199.

[23] Apollon multi-PW laser Users Facility, http://www.polytechnique.edu.

[24] A. Higginson, R. J. Gray, M. King, R. J. Dance, S. D. R. Williamson, N. M. H. Butler, R. Wilson, R. Capdessus, C. Armstrong, J. S. Green, S. J. Hawkes, P. Martin, W. Q. Wei, S. R. Mirfayzi, X. H. Yuan, S. Kar, M. Borghesi, R. J. Clarke, D. Neely, and P. McKenna, Near-100 MeV protons via a laser-driven transparency-enhanced hybrid acceleration scheme, Nat. Commun. **9,** 724 (2018).

[25] D. Haberberger, S. Tochitsky, F. Fiuza, C. Gong, R. A. Fonseca, L. O. Silva, W. B. Mori, and C. Joshi, Collisionless shocks in laser-produced plasma generate monoenergetic high-energy proton beams, Nat. Phys. **8,** 95 (2011).

[26] H. Zhang, B. Shen, W. Wang, S. Zhai, S. Li, X. Lu, J. Li, R. Xu, X. Wang, X. Liang, Y. Leng, R. Li, and Z. Xu, Collisionless Shock Acceleration of High-Flux Quasimonoenergetic Proton Beams Driven by Circularly Polarized Laser Pulses, Phys. Rev. Lett. **119,** 164801 (2017).

[27] A. Henig, S. Steinke, M. Schnürer, T. Sokollik, R. Hörlein, D. Kiefer, D. Jung, J. Schreiber, B. M. Hegelich, X. Q. Yan, J. M. ter Vehn, T. Tajima, P. V. Nickles, W. Sandner, and D. Habs, Radiation-Pressure Acceleration of ion Beams Driven by Circularly Polarized Laser Pulses, Phys. Rev. Lett. **103,** 245003 (2009).

[28] S. Kar, K. F. Kakolee, B. Qiao, A. Macchi, M. Cerchez, D. Doria, M. Geissler, P. McKenna, D. Neely, J. Osterholz, R. Prasad, K. Quinn, B. Ramakrishna, G. Sarri, O. Willi, X. Y. Yuan, M. Zepf, and M. Borghesi, Ion Acceleration in Multispecies Targets Driven by Intense Laser Radiation Pressure, Phys. Rev. Lett. **109,** 185006 (2012).

[29] J. Bin, W. Ma, H. Wang, M. Streeter, C. Kreuzer, D. Kiefer, M. Yeung, S. Cousens, P. Foster, B. Dromey, X. Yan, R. Ramis, J. M. ter Vehn, M. Zepf, and J. Schreiber, Ion Acceleration Using Relativistic Pulse Shaping in Near-Critical-Density Plasmas, Phys. Rev. Lett. **115,** 064801 (2015).

[30] C. Scullion, D. Doria, L. Romagnani, A. Sgattoni, K. Naughton, D. Symes, P. McKenna, A. Macchi, M. Zepf, S. Kar, and M. Borghesi, Polarization Dependence of Bulk ion Acceleration from Ultrathin Foils Irradiated by High-Intensity Ultrashort Laser Pulses, Phys. Rev. Lett. **119,** 054801 (2017).

[31] T. Esirkepov, M. Borghesi, S. V. Bulanov, G. Mourou, and T. Tajima, Highly Efficient Relativistic-Ion Generation in the Laser-Piston Regime, Phys. Rev. Lett. **92,** 175003 (2004).

[32] F. Pegoraro and S. V. Bulanov, Photon Bubbles and ion Acceleration in a Plasma Dominated by the Radiation Pressure of an Electromagnetic Pulse, Phys. Rev. Lett. **99,** 065002 (2007).

[33] A. Macchi, F. Cattani, T. V. Liseykina, and F. Cornolti, Laser Acceleration of ion Bunches at the Front Surface of Overdense Plasmas, Phys. Rev. Lett. **94,** 165003 (2005).

[34] M. Chen, A. Pukhov, T. P. Yu, and Z. M. Sheng, Enhanced Collimated gev Monoenergetic ion Acceleration from a Shaped Foil Target Irradiated by a Circularly Polarized Laser Pulse, Phys. Rev. Lett. **103,** 024801 (2009).

[35] T.-P. Yu, A. Pukhov, G. Shvets, and M. Chen, Stable Laser-Driven Proton Beam Acceleration from a Two-Ion-Species Ultrathin Foil, Phys. Rev. Lett. **105,** 065002 (2010).

[36] S. V. Bulanov, E. Y. Echkina, T. Z. Esirkepov, I. N. Inovenkov, M. Kando, F. Pegoraro, and G. Korn, Unlimited ion Acceleration by Radiation Pressure, Phys. Rev. Lett. **104,** 135003 (2010).

[37] L. Ji, A. Pukhov, and B. Shen, Ion acceleration in the 'dragging field' of a light-pressure-driven piston, New J. Phys. **16,** 063047 (2014).

[38] M. L. Zhou, X. Q. Yan, G. Mourou, J. A. Wheeler, J. H. Bin, J. Schreiber, and T. Tajima, Proton acceleration by single-cycle laser pulses offers a novel monoenergetic and stable operating regime, Phys. Plasmas **23,** 043112 (2016).

[39] Y. Wan, I. A. Andriyash, C. H. Pai, J. F. Hua, C. J. Zhang, F. Li, Y. P. Wu, Z. Nie, W. B. Mori, W. Lu, V. Malka, and C. Joshi, Ion acceleration with an ultra-intense two-frequency laser tweezer, New J. Phys. **22,** 052002 (2020).

[40] A. McIlvenny, D. Doria, L. Romagnani, H. Ahmed, N. Booth, E. J. Ditter, O. C. Ettlinger, G. S. Hicks, P. Martin, G. G. Scott, S. D. R. Williamson, A. Macchi, P. McKenna, Z. Najmudin, D. Neely, S. Kar, and M. Borghesi, Selective ion Acceleration by Intense Radiation Pressure, Phys. Rev. Lett. **127,** 194801 (2021).

[41] L. D. Landau and E. M. Lifshitz, *The Classical Theory of Fields* (Elsevier, Oxford, 1975).

[42] M. Tamburini, F. Pegoraro, A. Di Piazza, C. H. Keitel, and A. Macchi, Radiation reaction effects on radiation pressure acceleration, New J. Phys. **12,** 123005 (2010).

[43] M. Tamburini, F. Pegoraro, A. Di Piazza, C. H. Keitel, T. V. Liseykina, and A. Macchi, Radiation reaction effects on electron nonlinear dynamics and ion acceleration in laser-solid interaction, Nucl. Instrum. Methods Phys. Res., Sect. A **653,** 181 (2011).

[44] A. D. Piazza, C. Müller, K. Z. Hatsagortsyan, and C. H. Keitel, Extremely high-intensity laser interactions with fundamental quantum systems, Rev. Mod. Phys. **84,** 1177 (2012).

[45] J. M. Cole, *et al.*, Experimental Evidence of Radiation Reaction in the Collision of a High-Intensity Laser Pulse with a Laser-Wakefield Accelerated Electron Beam, Phys. Rev. X **8,** 011020 (2018).

[46] K. Poder, *et al.*, Experimental Signatures of the Quantum Nature of Radiation Reaction in the Field of an Ultraintense Laser, Phys. Rev. X **8,** 031004 (2018).

[47] M. Chen, A. Pukhov, T.-P. Yu, and Z.-M. Sheng, Radiation reaction effects on ion acceleration in laser foil interaction, Plasma Phys. Control. Fusion **53,** 014004 (2010).

[48] R. Capdessus and P. McKenna, Influence of radiation reaction force on ultraintense laser-driven ion acceleration, Phys. Rev. E **91,** 053105 (2015).

[49] F. Wan, K. Xue, Z.-K. Dou, K. Z. Hatsagortsyan, W. Yan, D. Khikhlukha, S. V. Bulanov, G. Korn, Y.-T. Zhao, Z.-F. Xu, and J.-X. Li, Imprint of the stochastic nature of photon emission by electrons on the proton energy spectra in the laser-plasma interaction, Plasma Phys. Control Fusion **61,** 084010 (2019).

[50] D. Seipt, D. D. Sorbo, C. P. Ridgers, and A. G. R. Thomas, Theory of radiative electron polarization in strong laser fields, Phys. Rev. A **98**, 023417 (2018).

[51] M. Büscher, A. Hützen, L. Ji, and A. Lehrach, Generation of polarized particle beams at relativistic laser intensities, High Power Laser Sci. Eng. **8**, e36 (2020).

[52] K. Xue, Z.-K. Dou, F. Wan, T.-P. Yu, W.-M. Wang, J.-R. Ren, Q. Zhao, Y.-T. Zhao, Z.-F. Xu, and J.-X. Li, Generation of highly-polarized high-energy brilliant γ-rays via laser-plasma interaction, Matter Radiat. Extremes **5**, 054402 (2020).

[53] Y.-F. Li, R. Shaisultanov, K. Z. Hatsagortsyan, F. Wan, C. H. Keitel, and J.-X. Li, Ultrarelativistic Electron-Beam Polarization in Single-Shot Interaction with an Ultraintense Laser Pulse, Phys. Rev. Lett. **122**, 154801 (2019).

[54] Y.-F. Li, R. Shaisultanov, Y.-Y. Chen, F. Wan, K. Z. Hatsagortsyan, C. H. Keitel, and J.-X. Li, Polarized Ultrashort Brilliant Multi-Gev γ Rays via Single-Shot Laser-Electron Interaction, Phys. Rev. Lett. **124**, 014801 (2020).

[55] W.-Y. Liu, K. Xue, F. Wan, M. Chen, J.-X. Li, F. Liu, S.-M. Weng, Z.-M. Sheng, and J. Zhang, Trapping and acceleration of spin-polarized positrons from γ photon splitting in wakefields, ArXiv:2011.00156.

[56] R.-T. Guo, Y. Wang, R. Shaisultanov, F. Wan, Z.-F. Xu, Y.-Y. Chen, K. Z. Hatsagortsyan, and J.-X. Li, Stochasticity in radiative polarization of ultrarelativistic electrons in an ultrastrong laser pulse, Phys. Rev. Res. **2**, 033483 (2020).

[57] T. D. Arber, K. Bennett, C. S. Brady, A. Lawrence-Douglas, M. G. Ramsay, N. J. Sircombe, P. Gillies, R. G. Evans, H. Schmitz, A. R. Bell, and C. P. Ridgers, Contemporary particle-in-cell approach to laser-plasma modelling, Plasma Phys. Control Fusion **57**, 113001 (2015).

[58] R. X. Li, Progress of the SULF 10 PW laser project, in *1st AAPPS-DPP Meeting*.

[59] A. Macchi, S. Veghini, and F. Pegoraro, "light Sail" Acceleration Reexamined, Phys. Rev. Lett. **103**, 085003 (2009).

[60] B. Qiao, M. Zepf, M. Borghesi, and M. Geissler, Stable GeV Ion-Beam Acceleration from Thin Foils by Circularly Polarized Laser Pulses, Phys. Rev. Lett. **102**, 145002 (2009).

[61] B. Qiao, M. Zepf, M. Borghesi, B. Dromey, M. Geissler, A. Karmakar, and P. Gibbon, Radiation-Pressure Acceleration of ion Beams from Nanofoil Targets: The Leaky Light-Sail Regime, Phys. Rev. Lett. **105**, 155002 (2010).

[62] F. Wan, Y. Wang, R.-T. Guo, Y.-Y. Chen, R. Shaisultanov, Z.-F. Xu, K. Z. Hatsagortsyan, C. H. Keitel, and J.-X. Li, High-energy γ-photon polarization in nonlinear breit-wheeler pair production and γ polarimetry, Phys. Rev. Res. **2**, 032049 (2020).

[63] L. H. Thomas, The motion of the spinning electron, Nature (London) **117**, 514 (1926).

[64] L. H. Thomas, The kinematics of an electron with an axis, Philos. Mag. **3**, 1 (1927).

[65] V. Bargmann, L. Michel, and V. L. Telegdi, Precession of the Polarization of Particles Moving in a Homogeneous Electromagnetic Field, Phys. Rev. Lett. **2**, 435 (1959).

[66] N. King, *et al.*, An 800-MeV proton radiography facility for dynamic experiments, Nucl. Instrum. Meth. A **424**, 84 (1999).

[67] W. Wang, C. Jiang, H. Dong, X. Lu, J. Li, R. Xu, Y. Sun, L. Yu, Z. Guo, X. Liang, Y. Leng, R. Li, and Z. Xu, Hollow Plasma Acceleration Driven by a Relativistic Reflected Hollow Laser, Phys. Rev. Lett. **125**, 034801 (2020).

[68] H. K. Avetissian, *Relativistic nonlinear electrodynamics: interaction of charged particles with strong and super strong laser fields*, Springer series in optical sciences, (Springer, New York, 2006), p. xiii, 333 p.

[69] E. Lindman and M. Stroscio, On the relativistic corrections to the ponderomotive force, Nucl. Fusion **17**, 619 (1977).

[70] B. Quesnel and P. Mora, Theory and simulation of the interaction of ultraintense laser pulses with electrons in vacuum, Phys. Rev. E **58**, 3719 (1998).

[71] F. Niel, C. Riconda, F. Amiranoff, R. Duclous, and M. Grech, From quantum to classical modeling of radiation reaction: A focus on stochasticity effects, Phys. Rev. E **97**, 043209 (2018).

[72] V. N. Baier, V. M. Katkov, and V. M. Strakhovenko, *Electromagnetic Processes at High Energies in Oriented Single Crystals* (World Scientific, Singapore, 1998).

[73] S. V. Bulanov, T. Z. Esirkepov, M. Kando, J. K. Koga, T. Nakamura, S. S. Bulanov, A. G. Zhidkov, Y. Kato, and G. Korn, in *High-Power, High-Energy, and High-Intensity Laser Technology; and Research Using Extreme Light: Entering New Frontiers with Petawatt-Class Lasers*, Vol. 8780, edited by G. Korn, L. O. Silva, and J. Hein, International Society for Optics and Photonics (SPIE, 2013), p. 185.

[74] N. Neitz and A. Di Piazza, Stochasticity Effects in Quantum Radiation Reaction, Phys. Rev. Lett. **111**, 054802 (2013).

[75] V. A. Vshivkov, N. M. Naumova, F. Pegoraro, and S. V. Bulanov, Nonlinear electrodynamics of laser pulse interaction with a thin foil, Phys. Plasmas **5**, 2727 (1998).

[76] S. S. Bulanov, E. Esarey, C. B. Schroeder, S. V. Bulanov, T. Z. Esirkepov, M. Kando, F. Pegoraro, and W. P. Leemans, Radiation pressure acceleration: The factors limiting maximum attainable ion energy, Phys. Plasmas **23**, 056703 (2016).